Frequency comb enhancement via the self-crystallization of vectorial cavity solitons

GRAEME N. CAMPBELL,[1,2] LEWIS HILL,[2] PASCAL DEL'HAYE,[2,3] AND GIAN-LUCA OPPO[1,*]

[1]*SUPA and Department of Physics, University of Strathclyde, Glasgow G4 0NG, Scotland, UK*
[2]*Max Planck Institute for the Science of Light, 91058 Erlangen, Germany*
[3]*Department of Physics, Friedrich-Alexander-Universität Erlangen-Nürnberg, 91058 Erlangen, Germany*
[*]*g.l.oppo@strath.ac.uk*

Abstract: Long-range interactions between dark vectorial temporal cavity solitons are induced by the formation of patterns via spontaneous symmetry breaking of orthogonally polarized fields in ring resonators. Turing patterns of alternating polarizations form between adjacent solitons, pushing them apart so that a random distribution of solitons along the cavity length spontaneously reaches equal equilibrium distances, the soliton crystal, without any mode crossing or external modulation. Enhancement of the frequency comb is achieved through the spontaneous formation of regularly spaced soliton crystals, 'self-crystallization', with greater power and spacing of the spectral lines for increasing soliton numbers. Partial self-crystallization is also achievable in long cavities, allowing one to build crystal sections with controllable numbers of cavity solitons separated by intervals of pattern solutions of, again, controllable length.

1. Introduction

The generation of optical frequency combs [1] is an active area of research due to the wide range of practical applications that span across various fields including telecommunication [2,3], spectroscopy [4,5] and quantum technologies [6]. Temporal cavity solitons (TCS) [7] can be key elements for broadband optical frequency combs [8]. TCS are a special class of cavity solitons that originate in dissipative optical resonators under the action of external driving, diffraction [9,10] and/or group velocity dispersion. Ring resonator geometries are now regularly used for the generation of optical frequency combs via TCS [1].

We consider a high finesse ring resonator composed of a Kerr medium, see Fig. 1, in the normal dispersion regime. A linearly polarized driving laser is coupled into the cavity, such that the intracavity fields may be resolved into components of orthogonal polarizations. In considering polarization components, vectorial TCSs display features in addition to those seen for a cavity with a single field, due to the possibility of spontaneous symmetry breaking (SSB) between polarization components [11]. The SSB of light within Kerr resonators has been demonstrated theoretically and experimentally where the intracavity field is composed of orthogonal polarized components [12–20], counterpropagaing components [21–29], a combination of the two [30–32], and most recently, between two, or more, coupled resonators [33–36]. We investigate the polarization properties of vectorial dark cavity solitons (VDS) in the normal dispersion regime and its effects on the formation of frequency combs. In particular, we present a useful 'self-crystallization' phenomenon in which an initially random distribution of VDSs spontaneously form a regular soliton crystal (RSC). Cavity soliton crystals were originally invented in [10] by using phase gradients to position them into regularly spaced structures. In the case of dispersion, the generation of RSCs has been previously demonstrated through perturbations introduced near avoided mode crossings [37–40], or an external modulation [41] of the field. Here, instead, we

present a new self-organization mechanism of long range interactions between adjacent VDSs via a SSB of Turing patterns capable to controllably generate RSC states.
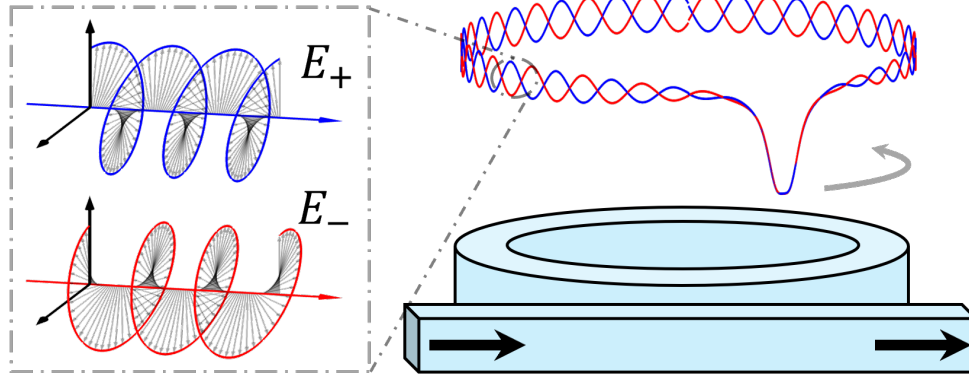
Fig. 1. A ring resonator composed of a Kerr nonlinear medium. Linearly polarised light is coupled in and out of the resonator via a waveguide. An example intracavity power profile of a vectorial soliton is shown, presenting a Turing pattern of broken symmetry between fields of opposite circular polarization, visible as out-of-phase oscillations in the background of the dark soliton pulse.

2. Model equations

We describe the propagation and coupling of the two orthogonal polarization modes in a ring resonator via coupled Lugiato-Lefever equations (LLE) [12,13,26,42–45]:

$$\partial_t E_\pm = S - (1 + i\theta)E_\pm + i(|E_\pm|^2 + 2|E_\mp|^2)E_\pm - i\partial_\tau^2 E_\pm, \tag{1}$$

where $E_\pm(\tau, t)$ are the slowly varying amplitudes of the two orthogonal polarization components of the field, S is the amplitude of the input field, considered to be real and positive, and θ is the input pump detuning to the near nearest cavity resonance. t is the 'slow time' temporal variable describing the evolution over many round trips of the cavity, while τ is the 'fast time' longitudinal variable describing the evolution over a single round trip of the cavity in the normal dispersion case with $0 \leq \tau \leq \tau_R$, where τ_R is the resonator round trip. Equations (1) are invariant under the exchange of the $+$ and $-$ indices, the fundamental symmetry of the system. Stationary solutions satisfying $E_+ = E_-$ are symmetric and $E_+ \neq E_-$ are symmetry broken.

Coupled LLE Eqs. (1) have been demonstrated to be extremely effective in describing the interaction of orthogonal polarization modes in fibre ring [12–14] and Fabry-Pérot [15] resonators. Although integrated optical resonators may have very different TE and TM modes, dual combs of polarized light have been realised in doped-silica-glass [46] and silicon nitride [47,48] microresonators, and successfully described via coupled LLE in [49,50]. Hence our analysis applies to a wide class of fibre and integrated ring resonators.

3. Homogeneous stationary solutions and Turing instabilities

We first provide a description of the SSB of the homogeneous stationary solutions (HSS) of Eqs. (1). The HSS of Eqs. (1) correspond to the two coupled equations

$$S^2 = H_\pm^2 - 2(\theta - 2H_\mp)H_\pm^2 + ((\theta - 2H_\mp)^2 + 1)H_\pm, \tag{2}$$

where $H_\pm = |E_{0,\pm}|^2$ is the power of the HSS $E_{0,\pm}$. In Fig. 2(a) we plot solutions of Eq. (2) for $S = 1.01, \tau_R = 150$. For this value of S there are only symmetric HSS ($H_+ = H_-$) which are
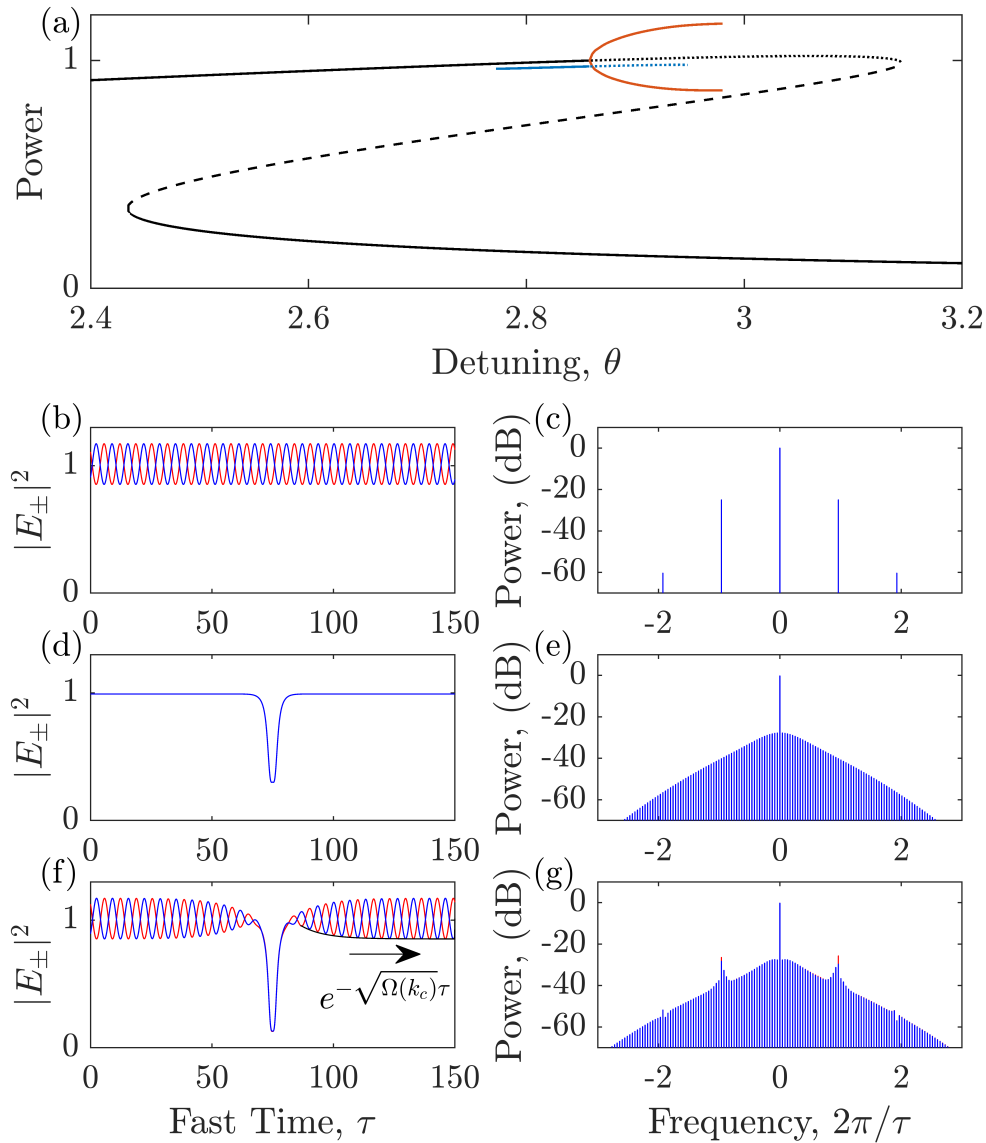
Fig. 2. Solutions of Eqs. (1) for $S = 1.01$, $\tau_R = 150$. (a) Stable (solid black curves) and unstable (broken black curves) symmetric homogeneous solutions, and stable (solid blue curves) and unstable (broken blue curves) symmetric single dark soliton solutions plotted as their average power. The maximum and minimum power of stable symmetry broken Turing pattern are also shown, in red. (b) Turing pattern of alternating polarization for $\theta = 2.94$ and (c) the corresponding frequency comb. (d) Power profile of symmetric dark soliton solutions for $\theta = 2.8$ and (e) the corresponding frequency comb. (f) Power profile of symmetry broken dark soliton solutions for $\theta = 2.94$ and (g) the corresponding frequency comb. The black curve in (f) outlines the envelope of the Turing pattern $\propto \exp\left(-\sqrt{\Omega(k_c)}\tau\right)$ as it approaches the vectorial dark soliton.

plotted as the black curve. In the parameter region of our interest there are no symmetry broken HSS solutions. The symmetric HSS form a tilted Lorentzian curve, where stable solutions are plotted with solid lines and and unstable solutions as broken lines. We note that Eqs. (1) have undergone extensive investigation in the absence of fast time effects [12,25,26,51].

Of key importance here is a Turing instability due to a SSB bifurcation of the high power bistable symmetric HSS typical of regimes of normal dispersion, resulting in the formation of a Turing pattern stationary state formed of alternating orthogonal polarizations. This supercritical bifurcation occurs when increasing the detuning and is plotted as a red curve depicting the maximum and minimum powers of the Turing pattern in Fig. 2(a). This instability is due to the field interaction through the cross-Kerr modulation and so it is not present on the high power HSS of a single LLE [52,53]. The Turing instability is found by considering perturbations on the HSS of the form $E_\pm = E_{0,\pm} + \epsilon_\pm e^{ik\tau + \Omega t}$ where k is the wavenumber of the perturbation and Ω is the slow time eigenvalue. The growth rate of this perturbation is then

$$\Omega(k) = -1 \pm \sqrt{\frac{-A_1 B_1 - A_2 B_2 \pm Q}{2}}, \qquad (3)$$

$$Q = \sqrt{(A_1 B_1 - A_2 B_2)^2 + 4A_1 A_2 C^2}, \qquad (4)$$

where $A_{1,2} = \theta - k^2 - H_\pm - 2H_\mp$, $B_{1,2} = \theta - k^2 - 3H_\pm - 2H_\mp$, $C^2 = 8H_+ H_-$. These eigenvalues have a similar form to the linear stability analysis of Refs. [25,26] where dispersion is neglected ($k = 0$). From these eigenvalues we may approximate the Turing wavenumber from the critical wavenumber with largest growth, $\Omega(k_c)$. For the example Turing pattern shown in Fig. 2(b) we find a good agreement between the predicted $k_c \approx 0.96$ and measured $k \approx 1.01$ wavenumber, although the value of θ is well above the Turing instability threshold.

4. Vectorial dark temporal cavity solitons

In the normal dispersion regime, Eqs. (1) exhibits VDSs [52]. These solutions are composed of localized switching fronts which connect the high and low power stable HSSs. Oppositely oriented pairs of switching fronts can 'lock' due to the interaction of local fast time oscillations close to the lower power plateau and become stationary VDS. This mechanism of soliton formation was first proposed for spatial solitons composed of diffractive switching fronts [54–56], but has been demonstrated longitudinally in the ring resonator with a single field component theoretically [52] and experimentally [57], as well as in Fabry-Pérot configurations [58].

First considering symmetric solitons, we note that at symmetry $E_+ = E_- = E$, Eqs. (1) reduce to

$$\partial_\tau E = S - (1 + i\theta)E + 3i|E|^2 E - i\partial_\tau^2 E. \qquad (5)$$

This means that under a re-normalization of fields $E \to E/\sqrt{3}$, $S \to S/\sqrt{3}$ the stationary VDS of our system are analogous to those of the LLE. A branch of symmetric solutions of Eqs. (1) containing a single VDS is shown in Fig. 2(a) as the blue curve (plotted as the average power over a round trip to separate it from the HSS). At this parameter value ($S = 1.01$) symmetric VDSs are stable for values of detuning below the Turing instability, shown in Figs. 2(d)–2(e). As the detuning is increased, the VDS symmetric solution undergoes a SSB of the homogeneous background from which the soliton hangs. This SSB results in the formation of a Turing pattern of alternating polarization components and is phenomenologically identical to the SSB of the HSS in the absence of the VDS.

The frequency comb of a symmetry broken VDS is shown in Fig. 2(g). It maintains a similar spectral envelope to that of the single symmetric VDS (Fig. 2(e)) but it develops sidebands due to the periodic modulations at the tails. The sideband peaks are reminiscent of those generated by dispersive waves due to higher order dispersion [59]. Here they are achieved with second order dispersion and the contribution of the Turing pattern modulation. The power and separation of these peaks correspond to the spectral lines of the frequency comb of the Turing pattern, Fig. 2(c).

An important property of symmetry broken VDSs is that the amplitude of the Turing pattern envelope decays as $[\exp(-\sqrt{\Omega(k_c)}\tau)]$, with $\Omega(k_c)$ given by Eq. (3), from the place where the VDS

tails are close to the unstable symmetric HSS to a saturation value of the modulated intensity. The black line in Fig. 2(f) shows this exponential decay matching the Turing pattern minima at the tails of the VDS. We have verified that such agreement persists over a wide range of detunings and input pumps where symmetry broken VDS are found.

## 5. Self-crystallization of temporal cavity solitons

We now consider solutions containing multiple VDSs along the cavity length simultaneously. After the SSB bifurcation, such solutions form Turing patterns in the intervals between VDSs. As the Turing patterns grow, adjacent VDS are 'pushed' apart until an equilibrium of the pattern's amplitude is reached on both sides of the VDS, as shown in Fig. 3. The formation of the symmetry broken Turing pattern is hence found to introduce long range repulsive interaction between adjacent VDSs. Note that the symmetric VDSs do not exhibit these long range interactions and the VDSs remain stationary at arbitrary separation distances.

In Fig. 3(a) we start with three symmetric VDSs randomly distributed along the round trip for $S = 1.02$, $\theta = 2.94$ and $\tau_R = 150$. For these parameter values, the homogeneous background is unstable to the formation of Turing pattern of alternating polarizations. The maximum amplitude reached by the Turing patterns in the intervals separating the VDSs depends on the separation of adjacent VDSs. As the pattern amplitude grows, the VDS are 'pushed' along the resonator until an equilibrium configuration of the pattern is reached on either side of each VDS. The slow time evolution of the three VDSs is shown in Fig. 3(c) through direct numerical integration of Eqs. (1). Here it can be seen that the VDSs move such as to spread out along the cavity coordinate. This evolution ends in the stationary state shown in Fig. 3(d) composed of VDSs located equidistantly on the round trip of the cavity and separated by Turing patterns equal amplitude, thus forming a perfect soliton crystal.

The formation of such a RSC induced by SSB evolves spontaneously from the initial condition of three randomly positioned dark solitons. The organization process corresponds to self-crystallization from a random distribution of VDSs. The RSCs of our system are robust to a change in the number of VDS as the repulsive interaction will redistribute VDS to equidistant locations, as long as the new RSC spacing is shorter than twice the characteristic Turing patterns saturation length $\Delta\tau$, defined as the fast time distance where the pattern amplitude reaches its maximum value.

As can be seen in Fig. 3(e), the RSC produces a frequency comb with a smooth spectral envelope and a spectral range three times larger than the frequency comb of the initial condition shown in Fig. 3(b). In general, a RSC composed of N VDSs produces a frequency comb equivalent to a single VDS in a cavity with round trip τ_R/N. The RSCs emulate smaller cavity sizes, such that with increasing soliton number, a frequency comb with enhanced power and greater spacing of the spectral lines is obtained. Due to these features, the spontaneous formation of RSC has many potential applications, such as satellite communications [60], photonic radar [61] and radio-frequency filters [62,63]. Being a self-organized structure, the RSC of our system offer different ways to generate and control RSCs than those demonstrated in Refs. [37,41]. As mentioned earlier, regular peaks in the spectral envelope are due to the Turing pattern wavenumber that is required for self-crystallization. Such peaks can be removed at will after self-crystallization by changing the control parameters across the SSB bifurcation, thus leaving a symmetric RSC with no pattern states between the VDS as shown for example in Fig. 3(f) and (g).

To demonstrate generality and robustness of the self-crystallization mechanism described above, we show in Fig. 4 the asymptotic results of simulations of Eqs. (1) for $S = 1.05$, $\theta = 3.0$ instead of $S = 1.02$, $\theta = 2.91$, and for one to six random VDSs in the initial condition obtained below the Turing threshold. These six configurations coexist and can be smoothly tuned by changes in the detuning θ. A further advantage of our method with respect to other techniques of generating RCSs, is that when adding or removing one of the VDSs through an external
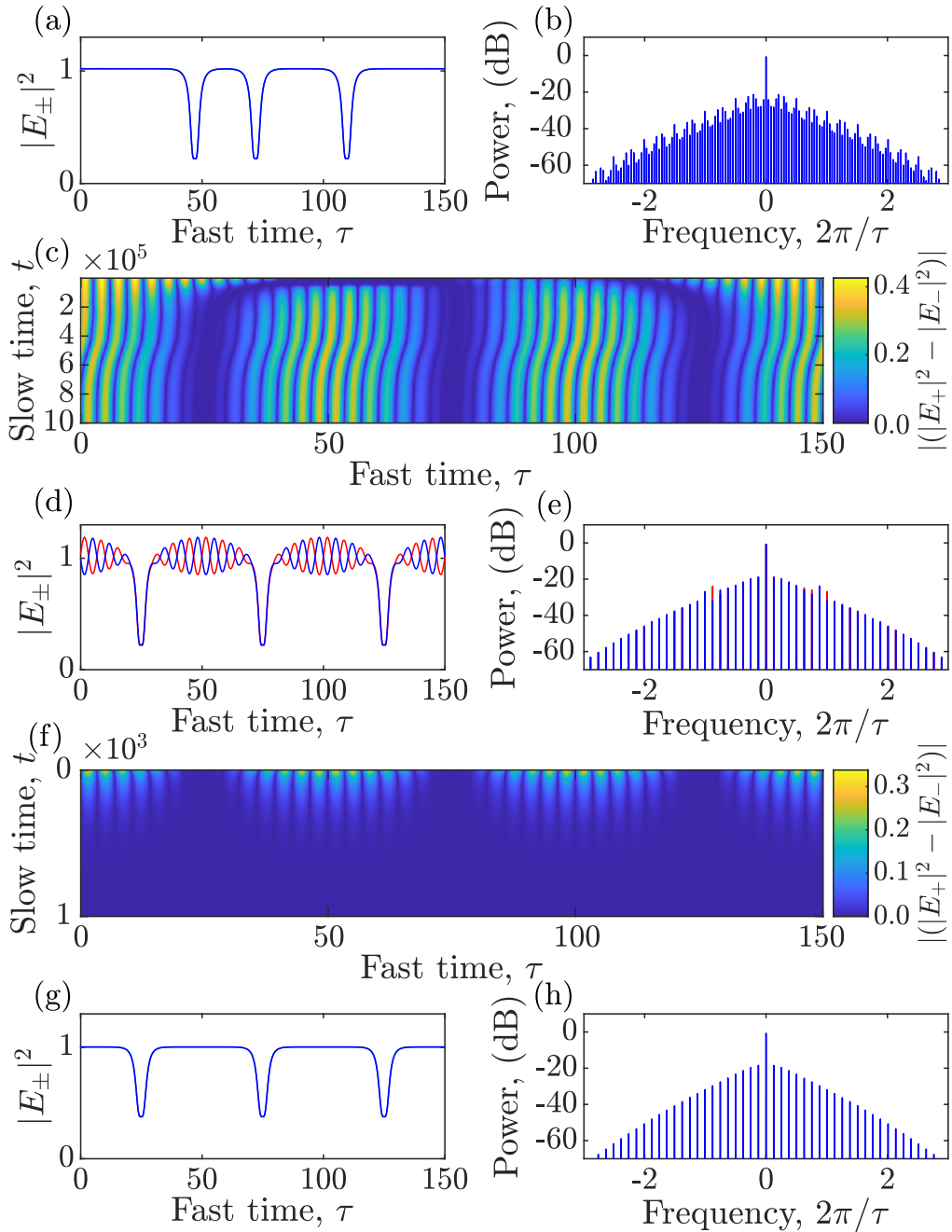
Fig. 3. (a) Initial condition of three symmetric vectorial dark solitons and corresponding comb spectrum (b). (c) Slow time evolution of the initial condition in (a) for $S = 1.02$, $\theta = 2.91$ demonstrating the growth of SSB Turing patterns, which propel the VDSs through the cavity. (d) Final RSC stationary state and corresponding comb spectrum (e). (f) Slow time evolution after reducing the cavity detuning to $\theta = 2.81$, below the threshold for Turing patterns. (g) Final regular VDS crystal with a uniform background and corresponding comb spectrum (h).
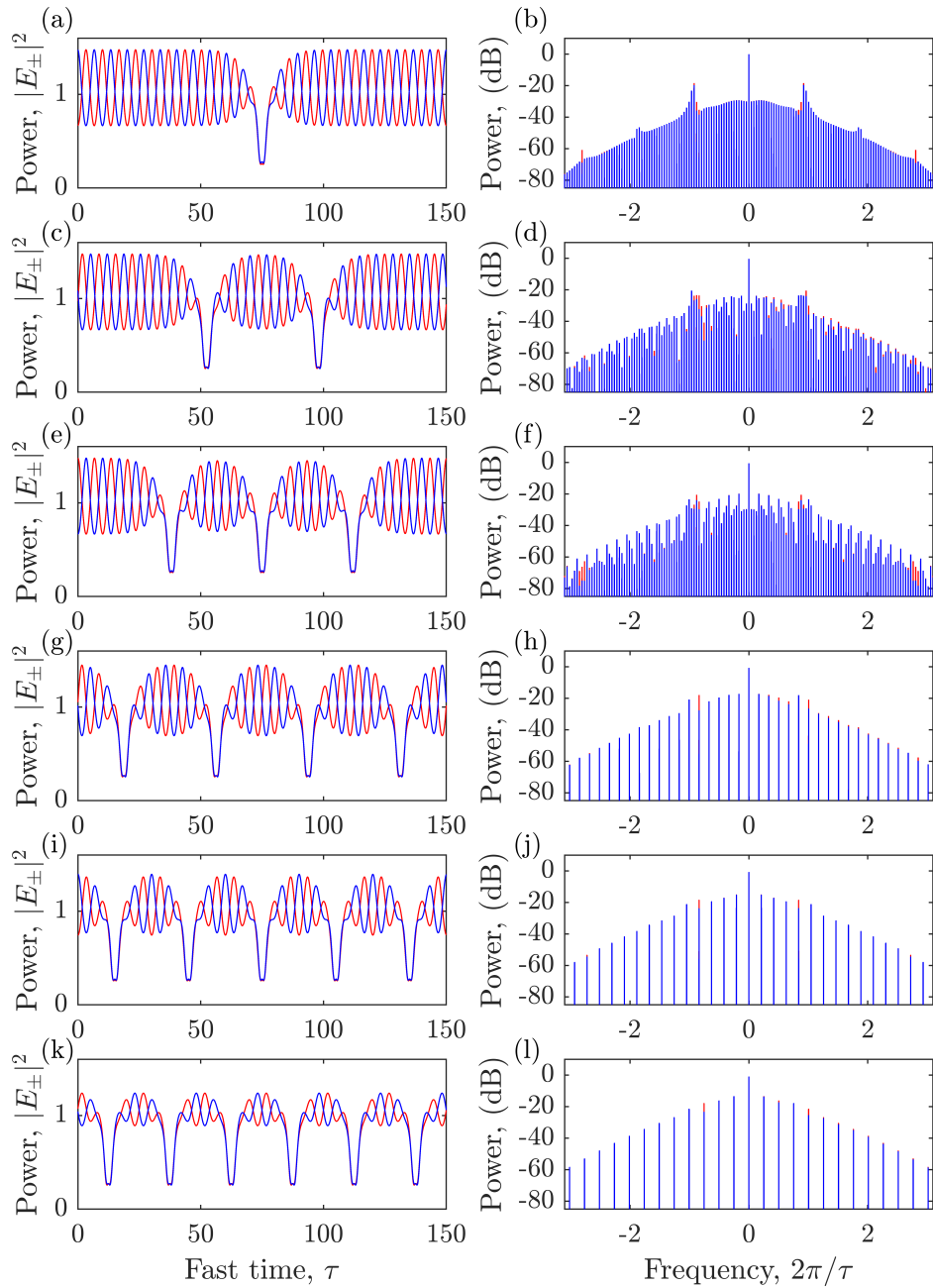
Fig. 4. A single (a) and five crystal states (c), (e), (g), (i), (k) for $S = 1.05$, $\theta = 3.0$. The initial conditions are randomly distributed VDSs leading to partial soliton crystals with two and three VDSs in (c) and (e), and to soliton crystals of four, five, and six VDSs in (g), (i) and (k), respectively. Panels (b), (d), (f), (h), (j) and (l) show the frequency comb spectra associated with each of the asymptotic VDS states.

perturbation, a crystal with an extra VDS or one less VDS smoothly nucleates via the long range interactions mediated by the Turing patterns.

On the right hand side of Fig. 4, we display the spectra corresponding to these asymptotic configurations. While periodic self-organised VDSs crystals are shown in (g), (i) and (k) for

four, five, and six VDSs, Figs. 4(c) and (e) show that self-crystallization may only happen in a section of the full cavity length as explained in the next section. We note that partial and/or full self-crystallization has been found within the parameter ranges of $(1.01 < S < 1.06)$, $(2.86 < \theta < 3)$ and $(150 < \tau_R < 300)$ with up to six VDSs coexisting with Turing patterns. This corresponds to tens of thousands of simulations and demonstrates the robustness, the wide range of occurrence and reproduction of our mechanism of self-crystallization of temporal cavity solitons. Note that self-crystallization is also observed when changing the cross-coupling and the dispersion coefficients here kept fixed to the values of 2 and 1, respectively.

6. Partial self-crystallization of temporal cavity solitons

Even in the case of a small number of VDSs in a long cavity, such as in Figs. 4(c) and (e) and in Fig. 5, VDSs are found to move apart until a saturation of the Turing pattern amplitude is reached in the intervals between them. In Fig. 5, five VDSs have undergone SSB, spread apart until the VDSs have become stationary and produced a local RSC via self-crystallization for $S = 1.04, \theta = 3$, (a)-(c) and for $S = 1.06, \theta = 3$, (b)-(d). The maximum range of the repulsive interaction between VDSs can be investigated using the growth rate, Eq. (3), of the critical wavenumber k_c of the Turing pattern away from the VDS. We are able to estimate the a maximum interaction distance $2\Delta\tau \approx -2\ln(0.01|E_{max}|^2)/\sqrt{\Omega(k_c)}$, where we have assumed the VDS interaction disappears when the Turing amplitude reaches 1% from the maximum amplitude $|E_{max}|^2$. This predicts a maximum lattice spacing of $2\Delta\tau \approx 37$ for $S = 1.04, \theta = 3$ and $2\Delta\tau \approx 31$ for $S = 1.06, \theta = 3$ compared to the measured values of 40 and 31 from Fig. 5, respectively. The interaction distance of VDSs can then be controlled by changing the control parameters to alter the growth rate of the Turing patterns. A pair of VDSs will no longer interact should
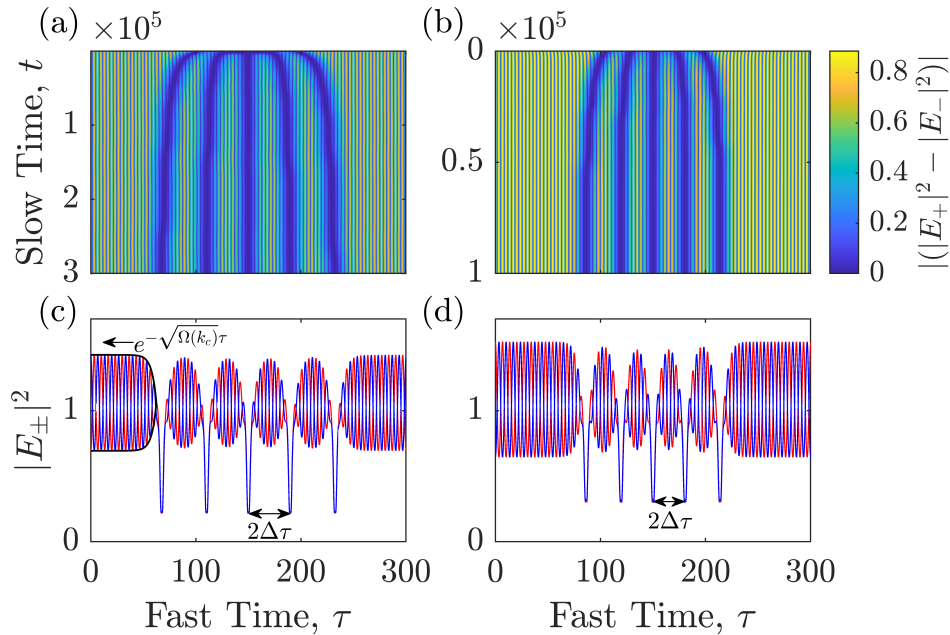
Fig. 5. Formation (a)-(b) and final partial soliton crystals (c)-(d) composed of five VDSs for $S = 1.04, \theta = 3$ (a)-(c) and $S = 1.06, \theta = 3$ (b)-(d). The VDS can move no closer than $2\Delta\tau$ due to the repulsive interactions induced by the Turing pattern. $2\Delta\tau \approx 40$ for (c) and $2\Delta\tau \approx 31$ for (d). The black curve in (c) follows the Turing pattern envelope starting from full saturation towards the VDS.
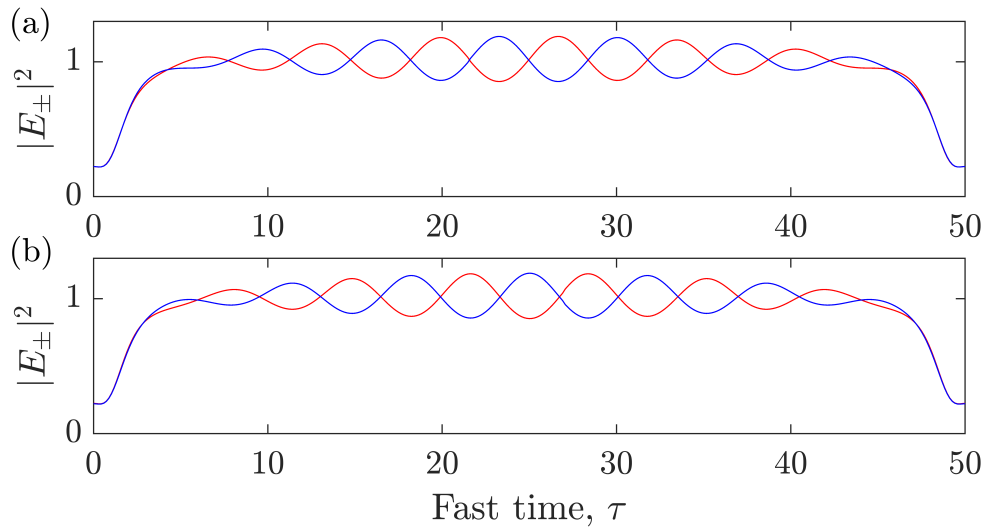
Fig. 6. (a)-(b) Power profiles of RSC unit cells for $S = 1.02, \theta = 2.91, \tau_R = 50N$. Two additional unit cells can be obtained by exchanging the fields $E_+ \leftrightarrow E_-$ in both (a) and (b). The unit cells are related by a phase shift in the peaks of the Turing patterns of $\pi/2$.

their separation be greater than $2\Delta\tau$ where the mediating Turing patterns reach saturation. By selecting a suitable cavity length and soliton number such that $N > \tau_R/2\Delta\tau$ we observe the full self-crystallization phenomenon as is shown in Fig. 3 and in Figs. 4(g), (i), (k).

RSCs are composed of a unit cell which is perfectly repeating over the cavity round trip. For example the RSCs of Fig. 3(d) and Figs. 4(g) and (k) are composed of the unit cell shown in Fig. 6(a) repeated several times over the round trip. The RCS of Fig. 4(i) is composed of a sequence of unit cells of the type shown in Fig. 6(b). These two unit cells possess the fast time symmetries $E_\pm(-\tau) = E_\mp(\tau)$ and $E_\pm(-\tau) = E_\pm(\tau)$ respectively, and two additional unit cells obtained by exchanging the fields $E_+ \leftrightarrow E_-$ in Fig. 6. As such, there are four possible RSCs, each related by an integer multiple phase shift of $\pi/2$ in the peaks of the Turing pattern. We find that all four RSCs are stable and can be reached depending on the initial condition. The system selection of one or the other type of cell strongly depends on the number of VDSs in the crystal and the ratio between the pattern wavelength and the cavity length.

If we return to Fig. 3 we see that the evolution of the three VDSs is composed of two regimes. For slow time $t < 3 \times 10^5$, the VDSs move apart due to the formation of the Turing patterns. At slow time $t \approx 3 \times 10^5$, the three VDSs approach an equal spacing in the cavity, but here the Turing pattern displays a non integer $\pi/2$ phase shift with respect to the stationary unit cells presented in Fig. 6. We now see transient dynamics in which the equidistant VDSs lattice and Turing pattern drift in fast time at different rates. This drift continues until one of the four stationary configurations is reached. We note the possibility of forming 'defective' crystals composed of alternating combinations of these four unit cells. Since the interest of this paper is about the novel method to generating soliton crystals which can be obtained with flat solutions separating the VDSs once one changes the detuning θ back below the Turing threshold (see Fig. 3(f) and (g)), we leave these and other matters related to pattern cells to future publications.

7. Conclusions

In conclusion, the formation of a RSC is achieved from a random distribution of VDSs via pattern formation with two field components of orthogonal polarization. SSB results in the

formation of Turing patterns of alternating polarization at the tails of the VDSs. Long range interactions between VDSs are induced and mediated by Turing patterns, which increase the separation between adjacent VDSs until an equidistant equilibrium distance is reached and a regularly spaced soliton crystal is formed. Although long range interactions can also be induced by local soliton oscillations [64] and field counter-propagation [51,65], our Turing pattern method offers new degrees of control, simple implementation, possible generalization to other systems with two or more interacting components, smooth transitions to crystals of larger or smaller numbers of cavity solitons and even tuning of the spatial interaction length resulting in localised crystallization. Moreover, in the regime of a Turing instability, RSCs originate spontaneously (self-crystallization) without the need of any perturbation [37–41] and represents a new, readily implementable, method for RSC formation relevant for applications [60–63]. RSCs produce a frequency comb displaying a smooth spectral profile and increased line spacing when compared to a random distribution of cavity solitons. As such, a RSC may be used to emulate smaller cavity sizes while avoiding the experimental limitations of small diameter ring resonators.

The same mechanism based on coexisting cavity solitons and Turing patterns can also lead to partial self-crystallization in long cavities such as those of fibre loops, allowing one to build crystal sections with controllable numbers of cavity solitons separated by intervals of pattern solutions (or flat solutions if one moves the detuning θ back below the Turing threshold) of, again, controllable length. The frequency combs obtained at the output of these configurations cannot be obtained from single small ring resonators of lengths comparable to twice the solitons distance $2\Delta\tau$ since these are always periodic. Quasicrystals, crystals with impurities and superpositions (periodic or random) of crystals of different lengths can be realised in an optical system to simulate and investigate solid state structures of difficult realization, i.e. photonic simulations. These come with the extra benefits of dual-mode operation and correlations. The self-crystallization mechanism described in this work is universal in systems displaying temporal cavity soltions and Turing instabilities and has already been generalized to Fabry-Pérot configurations with two orthogonal polarizations [30] We have also observed self-crystallization of VDSs in configurations of ring-resonators operating away from symmetric configurations that better describe integrated microresonators as those mentioned in [46–50].

Disclosures. The authors declare that there are no conflicts of interest related to this article.

Data availability. Data underlying the results presented in this paper are not publicly available at this time but may be obtained from the authors upon reasonable request.

References

1. A. Pasquazi, M. Peccianti, L. Razzari, *et al.*, "Micro-combs: a novel generation of optical sources," Phys. Rep. **729**, 1–81 (2018).
2. J. Pfeifle, V. Brasch, M. Lauermann, *et al.*, "Coherent terabit communications with microresonator Kerr frequency combs," Nat. Photonics **8**(5), 375–380 (2014).
3. J. Pfeifle, A. Coillet, R. Henriet, *et al.*, "Optimally coherent Kerr combs generated with crystalline whispering gallery mode resonators for ultrahigh capacity fiber communications," Phys. Rev. Lett. **114**(9), 093902 (2015).
4. M.-G. Suh, Q.-F. Yang, K. Y. Yang, *et al.*, "Microresonator soliton dual-comb spectroscopy," Science **354**(6312), 600–603 (2016).
5. A. Dutt, C. Joshi, X. Ji, *et al.*, "On-chip dual-comb source for spectroscopy," Sci. Adv. **4**(3), e1701858 (2018).
6. R. Christian, M. Kues, P. Roztocki, *et al.*, "Generation of multiphoton entangled quantum states by means of integrated frequency combs," Science **351**(6278), 1176–1180 (2016).
7. S. Coen and M. Erkintalo, "Temporal cavity solitons in Kerr media," in *Nonlinear Optical Cavity Dynamics: From Microresonators to Fiber Lasers* P. Grelu, ed., (John Wiley & Sons, 2015), pp. 11–40.
8. T. J. Kippenberg, R. Holzwarth, and S. A. Diddams, "Microresonator-based optical frequency combs," Science **332**(6029), 555–559 (2011).

9. A. J. Scroggie, W.J Firth, G.S McDonald, *et al.*, "Pattern formation in a passive Kerr cavity," Chaos, Solitons Fractals **4**(8-9), 1323–1354 (1994).

10. W. J. Firth and A. J. Scroggie, "Optical bullet holes: robust controllable localized states of a nonlinear cavity," Phys. Rev. Lett. **76**(10), 1623–1626 (1996).

11. D. N. Christodoulides and R. I. Joseph, "Vector solitons in birefringent nonlinear dispersive media," Opt. Lett. **13**(1), 53–55 (1988).

12. B. Garbin, J. Fatome, G.-L. Oppo, *et al.*, "Asymmetric balance in symmetry breaking," Phys. Rev. Res. **2**(2), 023244 (2020).

13. G. Xu, A. U. Nielsen, B. Garbin, *et al.*, "Spontaneous symmetry breaking of dissipative optical solitons in a two-component Kerr resonator," Nat. Commun. **12**(1), 4023 (2021).

14. G. Xu, L. Hill, J. Fatome, *et al.*, "Breathing dynamics of symmetry-broken temporal cavity solitons in Kerr ring resonators," Opt. Lett. **47**(6), 1486–1489 (2022).

15. N. Moroney, L. Del Bino, S. Zhang, *et al.*, "A Kerr polarization controller," Nat. Commun. **13**(1), 398 (2022).

16. L. Quinn, G. Xu, Y. Xu, *et al.*, "Random number generation using spontaneous symmetry breaking in a Kerr resonator," Opt. Lett. **48**(14), 3741–3744 (2023).

17. S. Coen, B. Garbin, G. Xu, *et al.*, "Nonlinear topological symmetry protection in a dissipative system," Nat. Commun. **15**(1), 1398 (2024).

18. L. Quinn, G. Xu, Y. Xu, *et al.*, "Towards a novel coherent Ising machine using symmetry breaking in a Kerr resonator," In *AI and Optical Data Sciences IV*, page PC1243806. SPIE, (2023).

19. J. Fatome, E. Lucas, B. Kibler, *et al.*, "Observation of polarization faticons in a fibre Kerr resonator," in *Conference on Lasers and Electro-Optics/Europe (CLEO/Europe 2023) and European Quantum Electronics Conference (EQEC 2023)*, paper pd_2_7, (2023).

20. T. Huang, H. Zheng, G. Xu, *et al.*, "Coexistence of nonlinear states with different polarizations in a Kerr resonator," Phys. Rev. A **109**(1), 013503 (2024).

21. A. E. Kaplan and P. Meystre, "Enhancement of the Sagnac effect due to nonlinearly induced nonreciprocity," Opt. Lett. **6**(12), 590–592 (1981).

22. A. E. Kaplan and P. Meystre, "Directionally asymmetrical bistability in a symmetrically pumped nonlinear ring interferometer," Opt. Comm. **40**(3), 229–232 (1982).

23. E. M. Wright, P. Meystre, W. J. Firth, *et al.*, "Theory of the nonlinear Sagnac effect in a fiber-optic gyroscope," Phys. Rev. A **32**(5), 2857–2863 (1985).

24. L. Del Bino, J. M. Silver, S. L. Stebbings, *et al.*, "Symmetry breaking of counter-propagating light in a nonlinear resonator," Sci. Rep. **7**(1), 43142 (2017).

25. M. T. M. Woodley, J. M. Silver, L. Hill, *et al.*, "Universal symmetry-breaking dynamics for the Kerr interaction of counterpropagating light in dielectric ring resonators," Phys. Rev. A **98**(5), 053863 (2018).

26. L. Hill, G.-L. Oppo, M. T. M. Woodley, *et al.*, "Effects of self-and cross-phase modulation on the spontaneous symmetry breaking of light in ring resonators," Phys. Rev. A **101**(1), 013823 (2020).

27. M. T. M. Woodley, L. Hill, L. Del Bino, *et al.*, "Self-switching Kerr oscillations of counterpropagating light in microresonators," Phys. Rev. Lett. **126**(4), 043901 (2021).

28. C. Cui, L. Zhang, and L. Fan, "Control spontaneous symmetry breaking of photonic chirality with reconfigurable anomalous nonlinearity," arXiv (2022).

29. R. D. D. Bitha, A. Giraldo, N. G. R. Broderick, *et al.*, "Bifurcation analysis of complex switching oscillations in a Kerr microring resonator," Phys. Rev. E **108**(6), 064204 (2023).

30. G. N. Campbell, L. Hill, G.-L. Oppo, *et al.*, "Dark temporal cavity soliton pairs in Fabry-Pérot resonators with normal dispersion and orthogonal polarizations," in *CLEO/Europe and EQEC*, paper ef_p_3, (2023).

31. L. Hill, E.-M. Hirmer, G. Campbell, *et al.*, "Symmetry broken vectorial kerr frequency combs from Fabry-Pérot resonators," Comm. Phys. **7**(1), 82 (2024).

32. L. Hill, G.-L. Oppo, and P. Del'Haye, "Multi-stage spontaneous symmetry breaking of light in Kerr ring resonators," Comm. Phys. **6**(1), 208 (2023).

33. Y. Rah and K. Yu, "Demonstration of spontaneous symmetry breaking in self-modulated ring resonators," Phys. Rev. Res. **6**(1), 013234 (2024).

34. K. W. Cheah, J. Mai, X. Huang, *et al.*, "Spontaneous symmetry breaking of non-Hermitian coupled nano-cavities," Research Square, (2023).

35. A. Ghosh, L. Hill, G.-L. Oppo, *et al.*, "Four-field symmetry breakings in twin-resonator photonic isomers," Phys. Rev. Res. **5**(4), L042012 (2023).

36. A. Ghosh, A. Pal, L. Hill, *et al.*, "Controlled light distribution with coupled microresonator chains via Kerr symmetry breaking," arXiv, (2024).

37. D. C. Cole, E. S. Lamb, P. Del'Haye, *et al.*, "Soliton crystals in Kerr resonators," Nat. Photonics **11**(10), 671–676 (2017).

38. W. Wang, Z. Lu, W. Zhang, *et al.*, "Robust soliton crystals in a thermally controlled microresonator," Opt. Lett. **43**(9), 2002–2005 (2018).

39. M. Karpov, M. H. P. Pfeiffer, H. Guo, *et al.*, "Dynamics of soliton crystals in optical microresonators," Nat. Phys. **15**(10), 1071–1077 (2019).

40. G. Lin and T. Sun, "Mode crossing induced soliton frequency comb generation in high-Q yttria-stabilized zirconia crystalline optical microresonators," Photoincs Res. **10**(3), 731–739 (2022).

41. L. Zhizhou, H.-J. Chen, W. Wang, *et al.*, "Synthesized soliton crystals," Nat. Commun. **12**(1), 3179 (2021).

42. L. A. Lugiato and R. Lefever, "Spatial dissipative structures in passive optical systems," Phys. Rev. Lett. **58**(21), 2209–2211 (1987).

43. M. Haelterman, S. Trillo, S. Wabnitz, *et al.*, "Dissipative modulation instability in a nonlinear dispersive ring cavity," Opt. Comm. **91**(5-6), 401–407 (1992).

44. L. A. Lugiato, F. Prati, M. L. Gorodetsky, *et al.*, "From the Lugiato-Lefever equation to microresonator-based soliton Kerr frequency combs," Phil. Trans. R. Soc. A. **376**(2135), 20180113 (2018).

45. J. B. Geddes, J. V. Moloney, E. M. Wright, *et al.*, "Polarisation patterns in a nonlinear cavity," Opt. Comm. **111**(5-6), 623–631 (1994).

46. W. Wang, W. Zhang, Z. Lu, *et al.*, "Self-locked orthogonal polarized dual comb in a microresonator," Photonics Res. **6**(5), 363–367 (2018).

47. C. Bao, P. Liao, A. Kordts, *et al.*, "Orthogonally polarized frequency comb generation from a Kerr comb via cross-phase modulation," Opt. Lett. **44**(6), 1472–1475 (2019).

48. Z. Wu, Y. Gao, T. Zhang, *et al.*, "Coexistence of multiple microcombs in monochromatically pumped Si_3N_4 microresonators," Opt. Lett. **47**(5), 1190–1193 (2022).

49. T. Hansson, M. Bernard, and S. Wabnitz, "Modulational instability of nonlinear polarization mode coupling in microresonators," J. Opt. Soc. Am. B **35**(4), 835–841 (2018).

50. R. Suzuki, S. Fujii, A. Hori, *et al.*, "Theoretical study on dual-comb generation and soliton trapping in a single microresonator with orthogonally polarized dual pumping," IEEE Photonics Journal **11**, 6100511 (2019).

51. G. N. Campbell, S. Zhang, L. Del Bino, *et al.*, "Counterpropagating light in ring resonators: Switching fronts, plateaus, and oscillations," Phys. Rev. A **106**(4), 043507 (2022).

52. P. Parra-Rivas, E. Knobloch, D. Gomila, *et al.*, "Dark solitons in the Lugiato-Lefever equation with normal dispersion," Phys. Rev. A **93**(6), 063839 (2016).

53. C. Godey, I. V. Balakireva, A. Coillet, *et al.*, "Stability analysis of the spatiotemporal lugiato-lefever model for Kerr optical frequency combs in the anomalous and normal dispersion regimes," Phys. Rev. A **89**(6), 063814 (2014).

54. N. N. Rosanov and G. V. Khodova, "Diffractive autosolitons in nonlinear interferometers," J. Opt. Soc. Am. B **7**(6), 1057–1065 (1990).

55. G.-L. Oppo, A. J. Scroggie, and W. J. Firth, "From domain walls to localized structures in degenerate optical parametric oscillators," J. Opt. B: Quantum Semiclassical Opt. **1**(1), 133–138 (1999).

56. G.-L. Oppo, A. J. Scroggie, and W. J. Firth, "Characterization, dynamics and stabilization of diffractive domain walls and dark ring cavity solitons in parametric oscillators," Phys. Rev. E **63**(6), 066209 (2001).

57. B. Garbin, Y. Wang, S. G. Murdoch, *et al.*, "Experimental and numerical investigations of switching wave dynamics in a normally dispersive fibre ring resonator," Eur. Phys. J. D **71**, 1–8 (2017).

58. G. N. Campbell, L. Hill, P. Del'Haye, *et al.*, "Dark solitons in Fabry-Pérot resonators with Kerr media and normal dispersion," Phys. Rev. A **108**(3), 033505 (2023).

59. S. Fujii and T. Tanabe, "Dispersion engineering and measurement of whispering gallery mode microresonator for Kerr frequency comb generation," Nanophotonics **9**(5), 1087–1104 (2020).

60. J. Federici and L. Moeller, "Review of terahertz and subterahertz wireless communications," J. Appl. Phys. **107**(11), 1 (2010).

61. J. Riemensberger, A. Lukashchuk, M. Karpov, *et al.*, "Massively parallel coherent laser ranging using a soliton microcomb," Nature **581**(7807), 164–170 (2020).

62. X. Xu, J. Wu, T. G. Nguyen, *et al.*, "Advanced RF and microwave functions based on an integrated optical frequency comb source," Opt. Express **26**(3), 2569–2583 (2018).

63. J. Hu, J. He, J. Liu, *et al.*, "Reconfigurable radiofrequency filters based on versatile soliton microcombs," Nat. Commun. **11**(1), 4377 (2020).

64. D. Turaev, A. G. Vladimirov, and S. Zelik, "Long-range interaction and synchronization of oscillating dissipative solitons," Phys. Rev. Lett. **108**(26), 263906 (2012).

65. H. Wang, B. Shen, Y. Yu, *et al.*, "Self-regulating soliton switching waves in microresonators," Phys. Rev. A **106**(5), 053508 (2022).